DØ note 3319
Draft Version 3.0
November 10, 1998

Study of the Run II Luminosity Monitor Counter Design

Chyi-Chang Miao and Richard Partridge

Abstract

We evaluate the Run II Luminosity Monitor counter design based on wedge-shaped scintillator elements with fine-mesh photomultiplier readout. Simulations of the Luminosity Monitor counters are used to study the light collection efficiency and position dependence for various counter options. The performance of fine-mesh photomultipliers in a magnetic field is studied using the DØ test beam facility, where we find the tubes provide the required gain and are able to make precise time-of-flight measurements in DØ's magnetic field. Prototype Luminosity Monitor counters were built and tested using cosmic rays. The intrinsic time resolution is measured to be 154 ps; including the degradation in time resolution due to the magnetic field and position dependence, we expect to achieve 269 ps time resolution for the Luminosity Monitor counters.

1 Introduction

In this note, we describe studies of prototype Luminosity Monitor counters based on scintillator wedges and fine-mesh photomultiplier readout. These studies include simulation results on the light collection efficiency and uniformity in response across the scintillator face, the performance of the fine-mesh photomultiplier readout in a magnetic field, and the time resolution of prototype counters.

Tube diameter	Photocathode diameter	No. of stages	Current amplification			Max. Anode Current
			B=0 T	B=0.5 T	B=1.0 T	
25.8 mm	17.5 mm	15	5×10^5	2.3×10^5	1.8×10^4	10 μA

Table 1: Characteristics of the Hamamatsu R5505 photomultiplier tube.

The note is organized as follows: In section 2, we briefly describe the layout of the proposed wedge design. A FORTRAN program was developed to simulate photon propagation in a scintillator wedge. Light collection efficiencies, uniformity of response, and photomultiplier pulse shapes are shown in section 3 for various design options. Test beam data were taken to evaluate the performance of the fine-mesh photomultiplier readout in a magnetic field. Measurements of photomultiplier gain and time resolution at various magnetic fields are described in section 4. Prototypes of wedge counters have been built and tested using cosmic rays with no magnetic field present. We describe the measurement of the time resolution for the counters on the cosmic ray test stand in section 5. We conclude in section 6.

2 Luminosity Monitor Design

In Run II, the Luminosity Monitor detector and readout will be mounted on the face of the endcap cryostats between the beam pipe and forward preshower detector. The assembly is not expected to exceed 10 cm in thickness, including photomultipliers, scintillator, and enclosure. This note focuses on a counter design where identical wedges of scintillator are symmetrically arranged about the beampipe in a “grapefruit” pattern. A 1” diameter fine-mesh photomultiplier is mounted on the face of each wedge near the center. The characteristics of the fine-mesh photomultiplier tube are briefly listed in Table 1.

Each scintillator wedge is 16.5 cm long, with the inner edge 3.2 cm from the beam axis. We have studied designs with segmentation of 24 and 32 scintillator wedges and scintillator thicknesses ranging from 0.5 to 1 inch. The two designs are shown in Figs. 1 and 2. To increase the light collection, we wrap the counters in a reflective material (aluminum foil in our prototype tests).

3 Simulations

We developed a simulation program to model the response of a single Luminosity Monitor counter to a charged particle passing through it. The charged particle produces excitations in the scintillator along its path, which then decay by radiating UV photons. Wavelength shifting compounds absorb the primary scintillation light, emitting photons in the blue region of the spectrum. We model this process by generating photons that are emitted isotropically at random points along the charged particle's path. The photon emission time is obtained using an exponential distribution with a 1.5 ns decay constant. The code thus does ray tracing of each of the photons in the counter, including the attenuation effect while photons traveling through the scintillator, and the total internal reflection when the emitted light strikes a surface. The output of the program are the estimation of the total transport time and the final photon status. The final photon status set in the program include

- photon entering the photomultiplier, which has an active area 17.5 mm in diameter centered 10.6 cm from the beam axis.
- photon absorbed by the scintillator wrapping
- photon absorbed by the scintillator itself

Various physical and detector constants are required to model the response. These include the speed of light, the scintillator index of refraction (1.58), the attenuation length (160 cm), the reflectivity of the wrapping (0.9), and the probability of an internally reflecting photon being absorbed due to surface imperfections (0.01 per reflection).

We generate thousands of photons at different positions along with the scintillator length to test the uniformity in time response and determine the photon collection efficiency. Counter designs with segmentation of 24 and 32 wedges are simulated for scintillator thicknesses of 0.5" and 1". We also simulated designs that absorb rather than reflect photons striking the outer edge of the scintillator furthest from the beam axis. Making this surface

	Scint. thickness	N	Position (cm)					Max/Min eff. ratio	σ_t (ps)
			-9.0	-4.5	0	3.7	7.3		
			Collection Efficiencies						
R	1.0"	24	4.8%	7.5%	24.0%	10.6%	10.0%	5.0	202
		32	5.7%	8.6%	26.4%	12.7%	12.1%	4.6	192
	0.5"	24	2.8%	4.5%	18.3%	6.7%	6.1%	6.5	182
		32	3.4%	5.2%	19.7%	8.1%	7.4%	5.8	173
NR	1.0"	24	2.4%	4.7%	21.4%	8.0%	7.1%	8.9	175
		32	2.9%	5.6%	23.6%	10.0%	9.0%	8.1	172
	0.5"	24	1.5%	3.1%	17.3%	5.6%	5.0%	11.5	158
		32	1.8%	3.7%	18.4%	7.0%	6.2%	10.2	157

Table 2: Simulation results on the photon collection efficiencies for different counter design options. Efficiencies for the 0.5" thick scintillator have been normalized by a factor of 1/2 for comparison. The options labeled with R have a reflector on the outer scintillator edge and those labeled NR have an absorber on this edge. N is the number of scintillator wedges. The coordinate system used has the photomultiplier at the origin with positive positions closer to the beam line. The contribution to the time resolution from the position dependence of the photon propagation time is given by σ_t.

absorbing prevents photons travelling radially outward from being reflected back towards the photomultiplier tube.

Simulation results show a large fraction of the photons are absorbed either by the wrapping or the scintillator itself, while less than 25% of the photons can enter the photomultiplier. Table 2 summarizes the results of the photon collection efficiency study. Listed are the acceptances at -9.0, -4.5, 0, 3.7, and 7.3 cm in a coordinate system where the origin is at the center of the photomultiplier with positive coordinates are closer to the beam axis. Note that photon collection efficiencies for 0.5" thick scintillator are listed with a normalization factor 1/2 for comparison with those of 1" thickness. It is seen that the photon collection efficiency is systematically larger for the 32 wedge design, which is expected since in this case the width of the counter more closely matches the photocathode diameter. Excluding the normalization factor, photon collection efficiencies are increased for 0.5" thick scintillator which can be attributed to the increased chance of entering the photomultiplier. There is also a loss in photon collection efficiency, particularly at large radii (-9.0 and -4.5 cm positions), when the outer edge is made absorbing rather than reflecting.

The ratio between the maximum and minimum photon collection efficiencies varies from 4.6 to 11.5. The largest part of this variation is due to very large efficiencies for charged particles that hit the scintillator in a small region underneath the photomultiplier tube. The Luminosity Monitor electronics will need to be able to handle the larger signal pulses without saturation, while maintaining high efficiency for the smaller signals.

The intrinsic time resolution of a scintillation counter (*i.e.*, the time resolution for charged particles hitting a single point on the scintillator) typically scales as $n_{pe}^{-1/2}$ where n_{pe} is the number of photoelectrons collected by the photomultiplier tube and is directly related to the photon collection efficiency. Therefore we expect to have the worst intrinsic time resolution at the scintillator wider end. In addition, there is a contribution to the time resolution due to charged particles hitting at different locations on the scintillator resulting in varying photon propagation times. For the counter designs being studied, we expect this position contribution to be larger than the intrinsic time resolution, so our goal will be to minimize the position contribution rather than maximize the number of photoelectrons.

Figure 3 shows the distribution of photon propagation times for the design option with 24 wedges of 1" scintillator and a reflector at the outer scintillator edge. As expected, photons generated just under the photomultiplier have the smallest propagation delay and the sharpest profile. It is also seen that there is a second peak in the photon propagation time distribution for charged particle hits closest to the beam line (x = 3.7, 5.5, and 7.3 cm). This second peak corresponds to photons propagating to the outer edge of the scintillator and being reflected back to the photomultiplier tube. By making the outer edge an absorber (*i.e.*, paint it black) we can eliminate these reflections, as shown in Fig. 4.

To understand how the time resolution is affected by the position dependence in the photon propagation time, we have simulated the pulse shape from the photomultiplier tube. We have included in our model the emission time distribution of the scintillator (1.5 ns decay time), the photon propagation time from above, the transit time spread of the photomultiplier (FWHM

$= 0.35$ ns), and the response of the photomultiplier to a single photoelectron (Gaussian pulse shape with $\sigma = 1$ ns). Figure 5 shows the expected photomultiplier pulse shapes for various hit positions. The pulse shapes are almost indistinguishable except for a time delay that is found to track with the average photon propagation delay. Thus, we can estimate the contribution to the time resolution due to the position dependence by weighting the average photon propagation time with the charged particle density $dN/dr \propto 1/r$.

The position contribution to the time resolution is given by σ_t in Table 2. By changing the outside edge from a reflector to an absorber, the variation in average propagation time is reduced and the time resolution is improved as expected. Decreasing the scintillator thickness to 0.5" further improves the time resolution. We attribute this improvement to photons striking the front and rear faces of the scintillator more often, resulting in: (1) increased chance of hitting the photocathode at an early time, and (2) increased chance that photons taking a long path to the photocathode will be absorbed in a surface reflection or attenuated.

4 Test Beam Results

We have tested the performance of fine-mesh photomultiplier tubes in a magnetic field using the DØ test beam facility at NWA. The goal of these tests is to verify that the photomultiplier readout can achieve expected current amplification variation shown in Table 1 and determine the effect of the magnetic field on the time resolution.

The Luminosity Monitor counters are too large for the bore of the test beam magnet, so we built two test counters with 1" fine-mesh photomultipliers mounted on the side of hexagonal pieces of scintillator. The photomultipliers were aligned with the magnetic field and the counters were positioned so that beam particles passed through both counters.

The photomultiplier signals were attenuated at low magnetic fields to avoid large variations in the amplitude of the photomultiplier signal. The signals were then amplified using a Lecroy 612 NIM amplifier and discriminated at a 30 mV threshold to create a timing pulse. A CAMAC TDC and ADC were used to measure the time and charge of the photomultiplier signals.

With the photomultiplier high voltage set at 2000 V, we took runs with the magnetic field at 0, 0.2, 0.4, 0.6, 0.8, 0.9, 1.0, 1.1 and 1.2 Tesla. We also took runs with the photomultiplier high voltage set at 2300 V in a 1.0 Tesla field for two different levels of attenuation on the photomultiplier signals.

Figure 6 shows the relative gain of the two fine-mesh photomultiplier tubes as a function of the magnetic field. These results are in good agreement with the Hamamatsu data sheet, which indicates a relative gain of 3.6% gain in a 1 Tesla field.

The TDC and ADC information are used to measure the charged particle arrival time for both counters. To take into account of charge slewing effects, we calculate the arrival time as follows:

$$t_i = t_i^0 + s \cdot TDC_i + K_i/\sqrt{ADC_i}$$

where t_i^0 are the time offsets, $s = 0.05$ nsec/count is common to both counters, and K_i determine the size of the charge slewing correction. Note that since we are only interested in the time difference time difference $t_1 - t_2$, t_1^0 can be arbitrarily set to 0. We obtain $t_1^0 - t_2^0$ and K_i by minimizing $(t_1 - t_2)^2$. The time difference $(t_1 - t_2)$ distribution is then fit to a Gaussian; the width of the time difference distribution is expected to be $\sqrt{2}\sigma_t$ where σ_t is the time resolution of the counter.

Figure 7 shows the time resolution for the different runs. Substantial variation in the time resolution is seen, especially for the two runs with the photomultiplier high voltage set at 2300 V. We found that the time resolution was highly correlated with the average charge recorded by the ADC, with small signals giving much poorer time resolution as shown in Fig. 8. The source of this effect was traced to one of the Lecroy amplifier channels having a large amount of noise on its output.

To determine the effect of the noisy amplifier channel, we took a series of runs with the counters positioned in the beam behind the solenoid and attenuators used to vary the amplitude of the PMT signals. Figure 9 shows the $(time\ resolution)^2$ as a function of $\langle Q \rangle^{-2}$ for both the noisy amplifier channel and a good amplifier channel in the same module, where Q is the average ADC count of the two counters. We see the noise contribution to the $(time\ resolution)^2$ has two parts: one part is proportional to $\langle Q \rangle^{-2}$, as expected for a signal with a fixed rise time, and a second part that is a constant independent of the amplitude of the signal. Therefore the distribution for the noisy amplifier channel was fit into two straight lines to get the best estimation on the dependences. The contribution proportional to $\langle Q\rangle^{-2}$ is estimated as the corresponding slope of the line multiplied by the average ADC count of data point. And the constant part is estimated as the difference between the intersection of the fitting lines of noisy and good amplifier channels.

Figure 10 shows the corrected time resolution after removing the noise contribution. The effect of the magnetic field on the time resolution is estimated to be $(41 \pm 41)\%$ for a magnetic field of 1 Tesla. Since we expect that the magnetic field only affects the time resolution by through changes in the photoelectron collection efficiency, the above increase in time resolution should be independent of the counter used and is used in the next section to predict the time resolution of the Luminosity Monitor counters in the 1 Tesla field.

5 Prototype Test

We have built prototype counters for the designs with segmentation of 24 and 32 wedges. These prototypes differ somewhat in the scintillator length, thickness, and type. The 32 segment prototype uses 6.8" long, 1.0" thick Bicron BC-404 scintillator, while the 24 segment prototype uses 6.5" long, 5/8" thick Bicron BC-408 scintillator. A cosmic ray test stand was built to measure the time resolution of the prototype counters. The counter to be tested is placed between two sets of reference scintillation counters with photomultiplier readout on both ends. A coincidence of the four photomultiplier tubes on the reference counters provides a trigger for the test stand. The time difference between the two ends of the counters is used to define the position where the cosmic ray hit the reference counter, while the average of the times is used to determine the arrival time of the cosmic ray. Thus, the test stand can predict both the location where the cosmic ray hit the counter being tested as well as the time when it was hit.

Figure 11 shows the distribution of half the difference between the two measurements of the cosmic ray arrival time from the two reference counters. The width of this distribution, 56 ps, is the time resolution of the test stand. Similar resolutions are seen in every prototype test.

The time resolution of the prototype counter is measured by comparing the recorded time with the time predicted by the reference counters. We tested the 32 segment prototype counter with a reflector and an absorber on the outer scintillator edge. Figure 12 shows time resolution of 257 ps (231 ps) are obtained with a reflector (absorber) on the outer edge. As predicted by the simulation studies, the absorber option has better time resolution. In the rest of this section, we will only show results for counters with an absorber on the outer edge.

Figure 13 shows a time resolution of 225 ps for the 24 segment design, which is comparable to what is seen for the 32 segment design. Simulation studies predict a smaller position contribution to the time resolution for this design due to its shorter length and thinner scintillator, while the intrinsic time resolution should be somewhat worse due to a reduced number of photoelectrons and a somewhat slower scintillator.

The difference between the predicted and measured times as a function of hit position is shown in Fig. 14. The prototype tests are overlaid with the predictions of the simulation program and show good agreement. The intrinsic time resolution found by selecting events in a narrow band at the wider end of the scintillator and measuring the time resolution. For the 24 segment counter, we find an intrinsic time resolution of 154 ps with no magnetic field as shown in Fig. 15. Including the effect of a magnetic field and the position dependence from the simulation studies, we expect to achieve a time resolution of 269 ps for this counter design.

We also measured the photomultiplier gain for the tubes used in the measurement. The gain of the photomultiplier was determined by measuring the width of an LED pulsed to give $\approx$ 100 photoelectrons. Since the relative width of the charge distribution is given by $n_{pe}^{-1/2}$, we know the number of photoelectrons and the resulting charge, and a gain of 8.9×10^5 is obtained. Having obtained the gain of the photomultiplier, we can convert the measured charge from the prototype counter to the number of photoelectrons. The number of photoelectrons is shown in Figs. 16 and 17 for 32 segment prototype counters with reflecting and absorbing outer edges, respectively. Figure 18 shows the results for the 24 segment prototype with an absorbing outer edge. The number of photoelectrons can be predicted from the energy loss in plastic scintillator (2 MeV/cm), scintillation efficiency (1 photon/100 eV), the light collection efficiency, and the quantum efficiency of the photomultiplier tube (0.2). The simulation results are overlaid on the data in Figs. 16-18 and show excellent agreement. Note that it was necessary to rescale the measured hit position, whose distribution extends beyond the physical limits of the counter due measurement errors, to the length of the counter in order to make a sensible comparison.

6 Conclusion

We have studied the run II luminosity monitor counter design with scintillator wedges and fine-mesh photomultiplier readout. Both the 24 segment and 32 segment designs were studied using simulations and prototype tests. The fine-mesh photomultiplier readout is shown to be able to operate with high gain and good timing resolution in the 1 Tesla magnetic field. We achieve a timing resolution of 224 ps for a prototype counter for the 24 segment design with 5/8" thick BC-408 scintillator. A time resolution of 269 ps is predicted for this counter design operating at DØ.

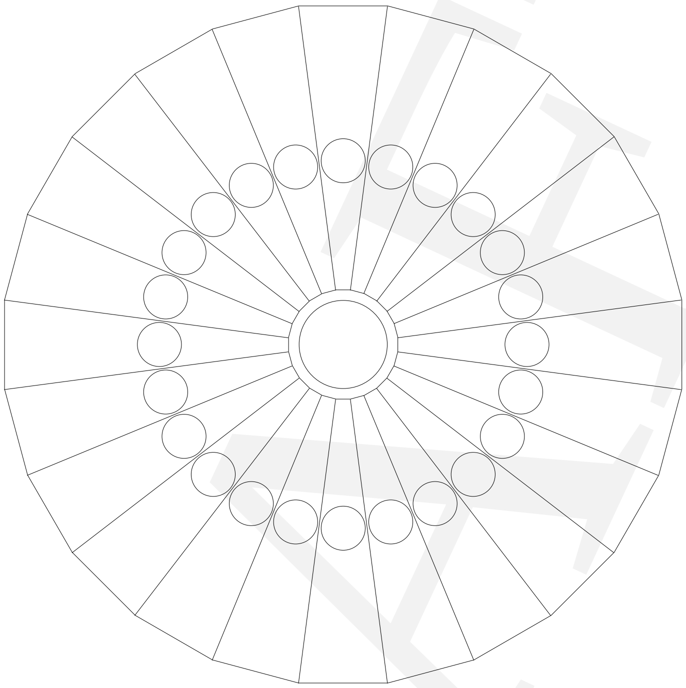

Figure 1: Luminosity Monitor design with 24 scintillator wedges and fine-mesh photomultiplier readout.

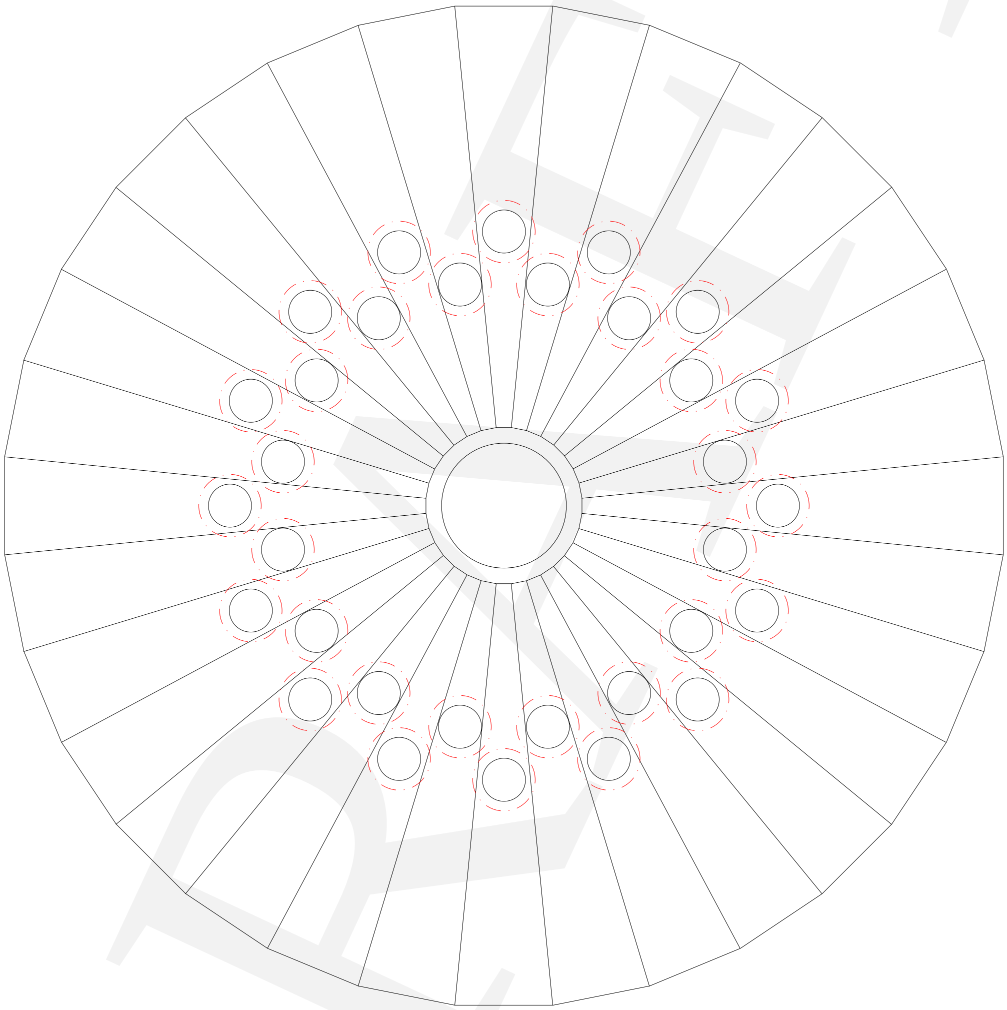

Figure 2: Luminosity Monitor design with 32 scintillator wedges and fine-mesh photomultiplier readout.

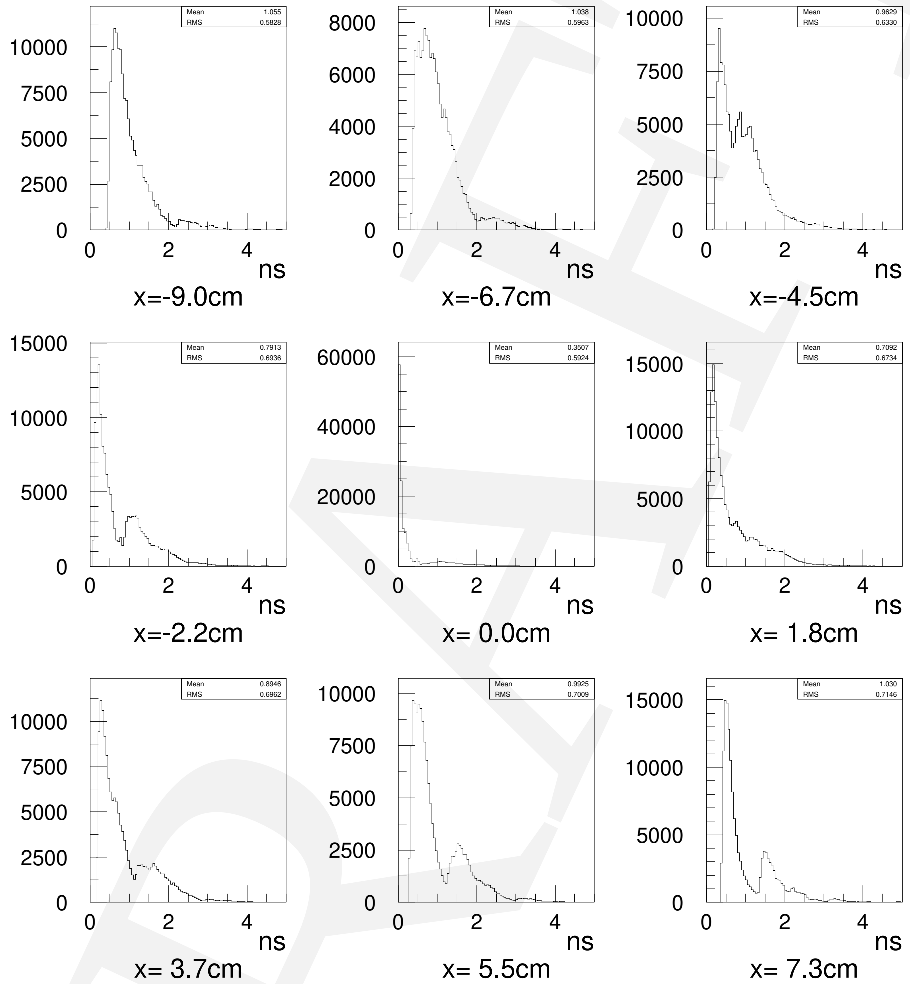

Figure 3: Photon propagation time for photons generated at different positions for the 24 segment design with a reflector on the outer scintillator edge. All plots are normalized to equal area.

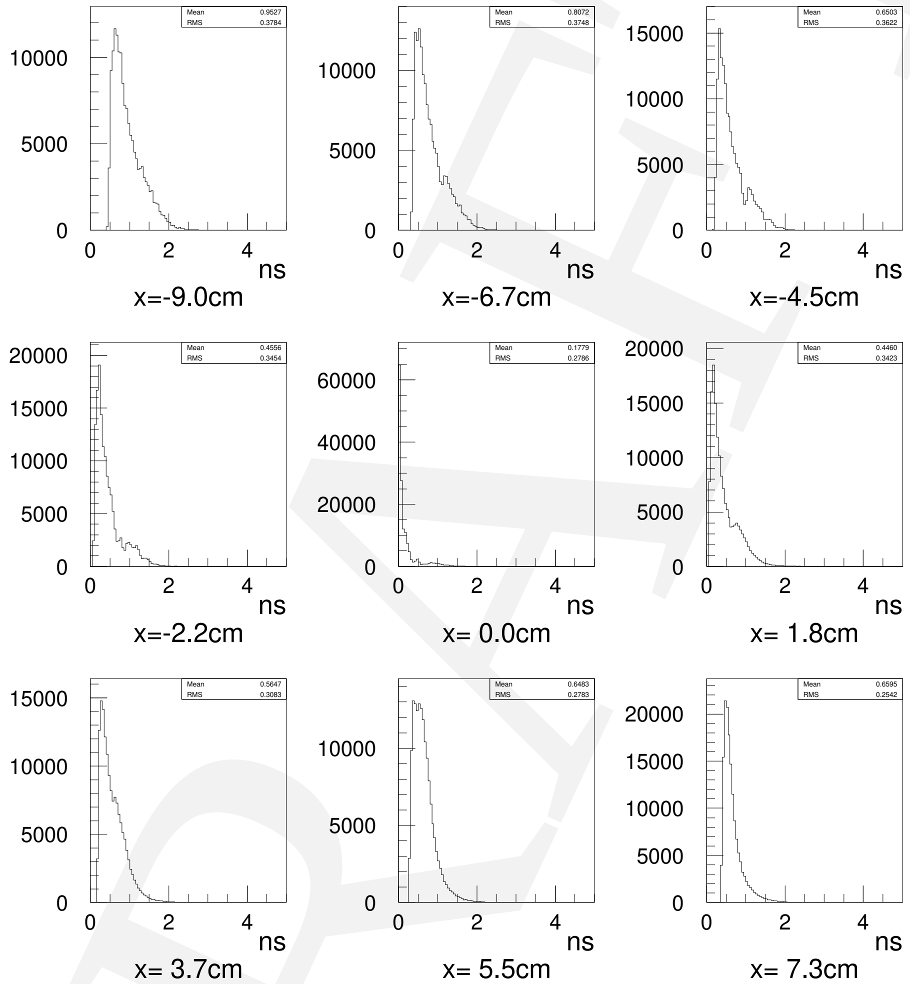

Figure 4: Photon propagation time for photons generated at different positions for the 24 segment design in an absorber at the outer scintillator edge. All plots are normalized to equal area.

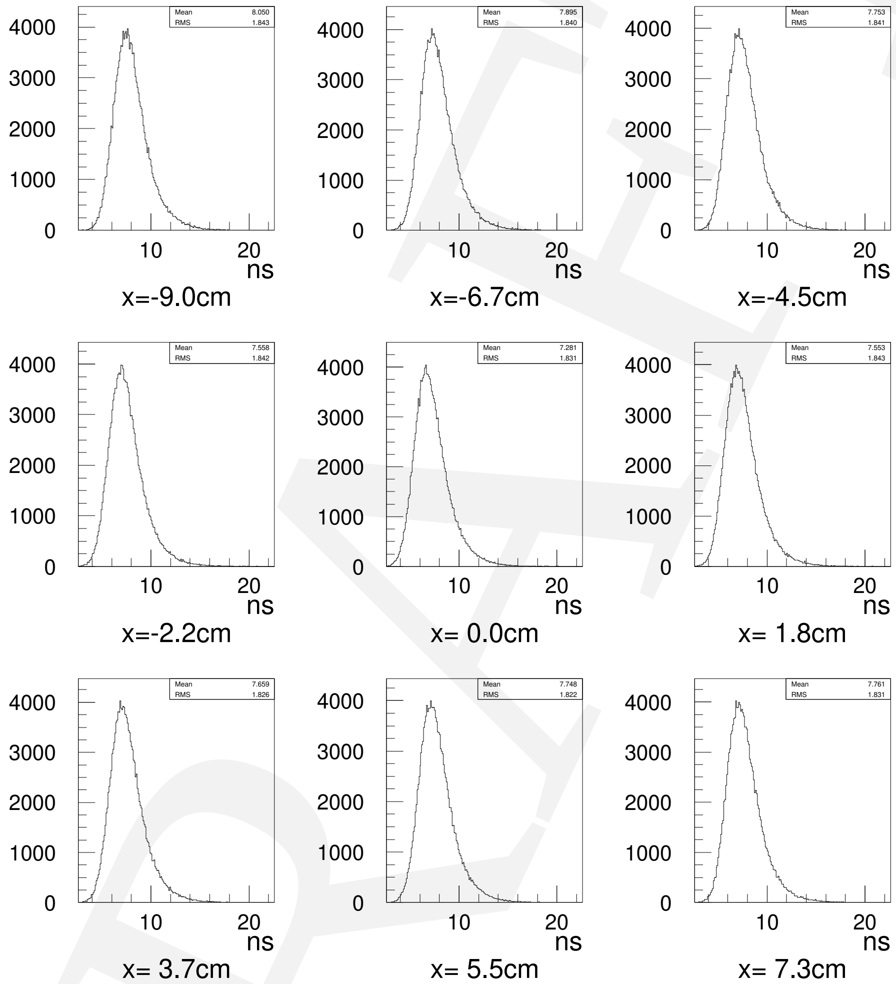

Figure 5: Photomultiplier pulse shape for photons generated at different positions for 24 segment design with an absorber at the outer scintillator edge. All plots are normalized to equal area.

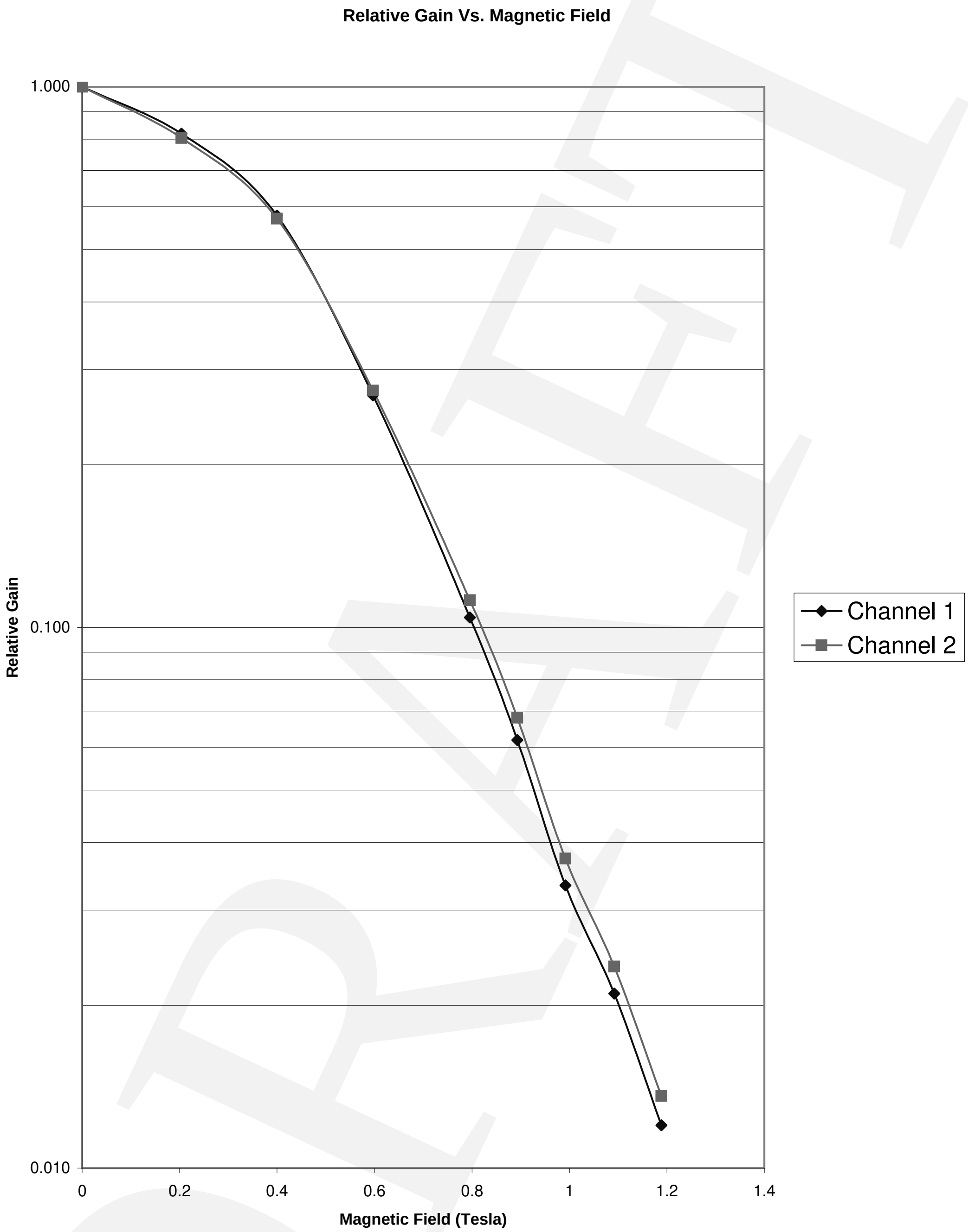

Figure 6: Relative gain vs. magnetic field for 1" fine-mesh photomultipliers.

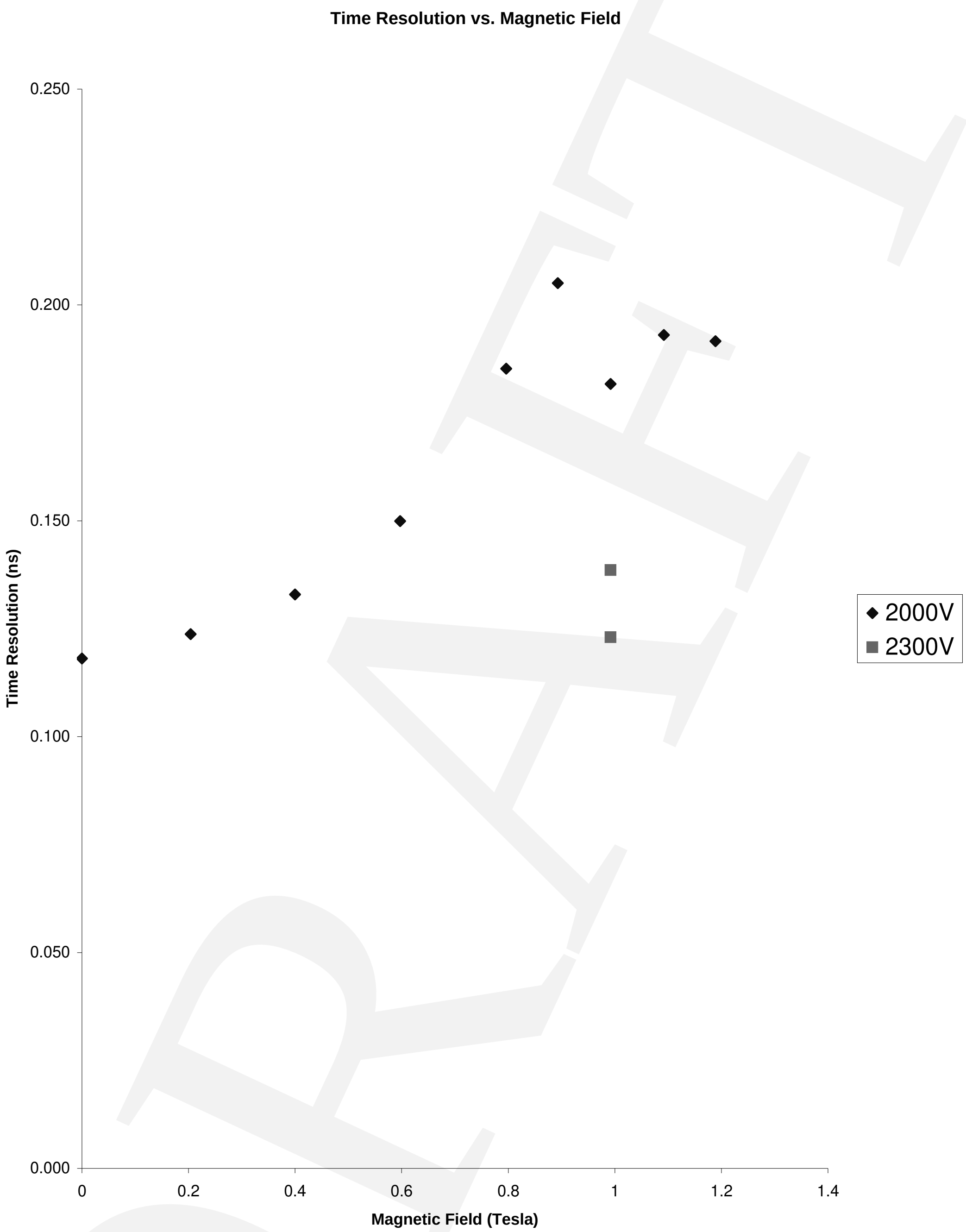

Figure 7: Time resolution vs. magnetic field for test counter before amplifier noise correction.

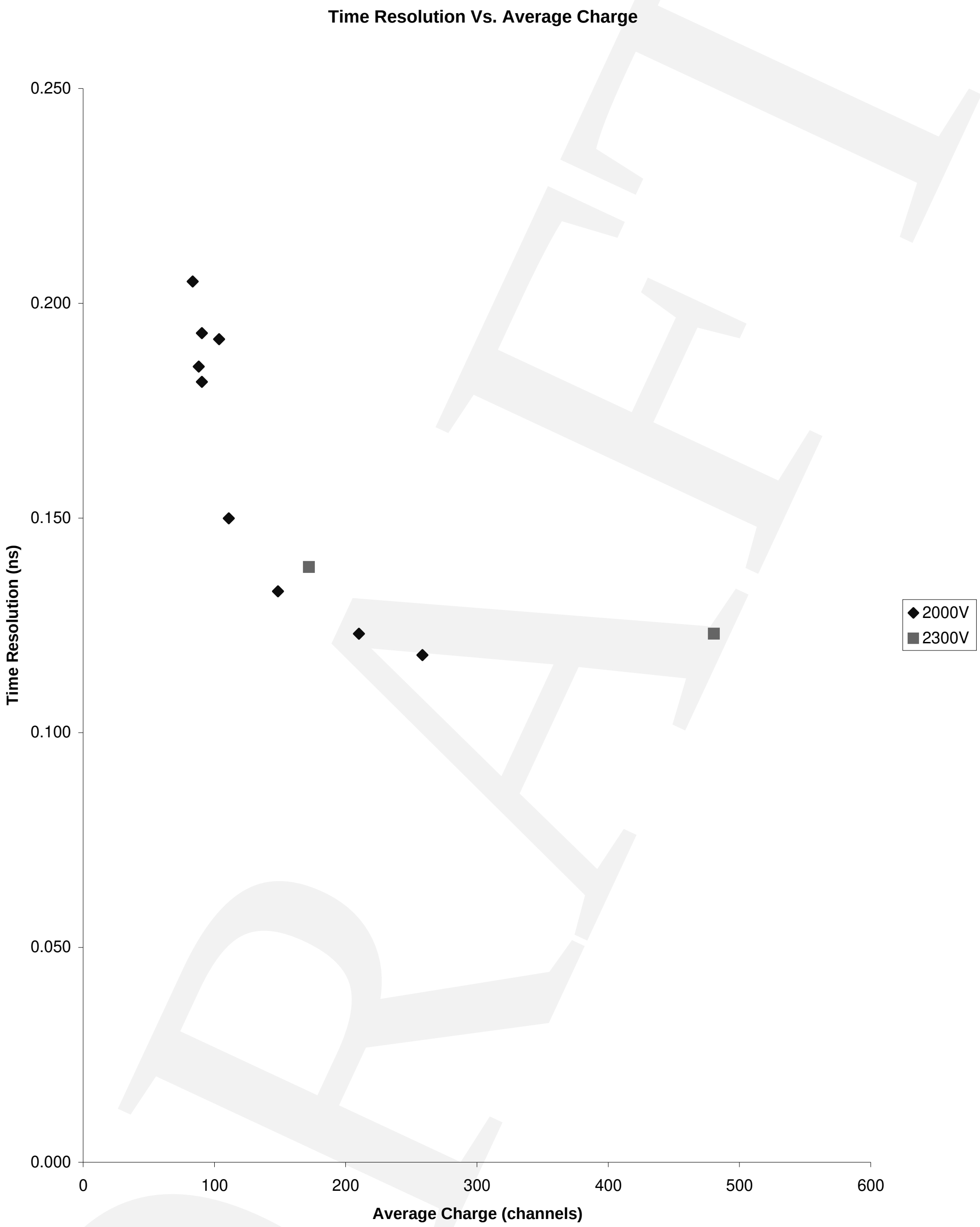

Figure 8: Time resolution vs. average charge for test counter.

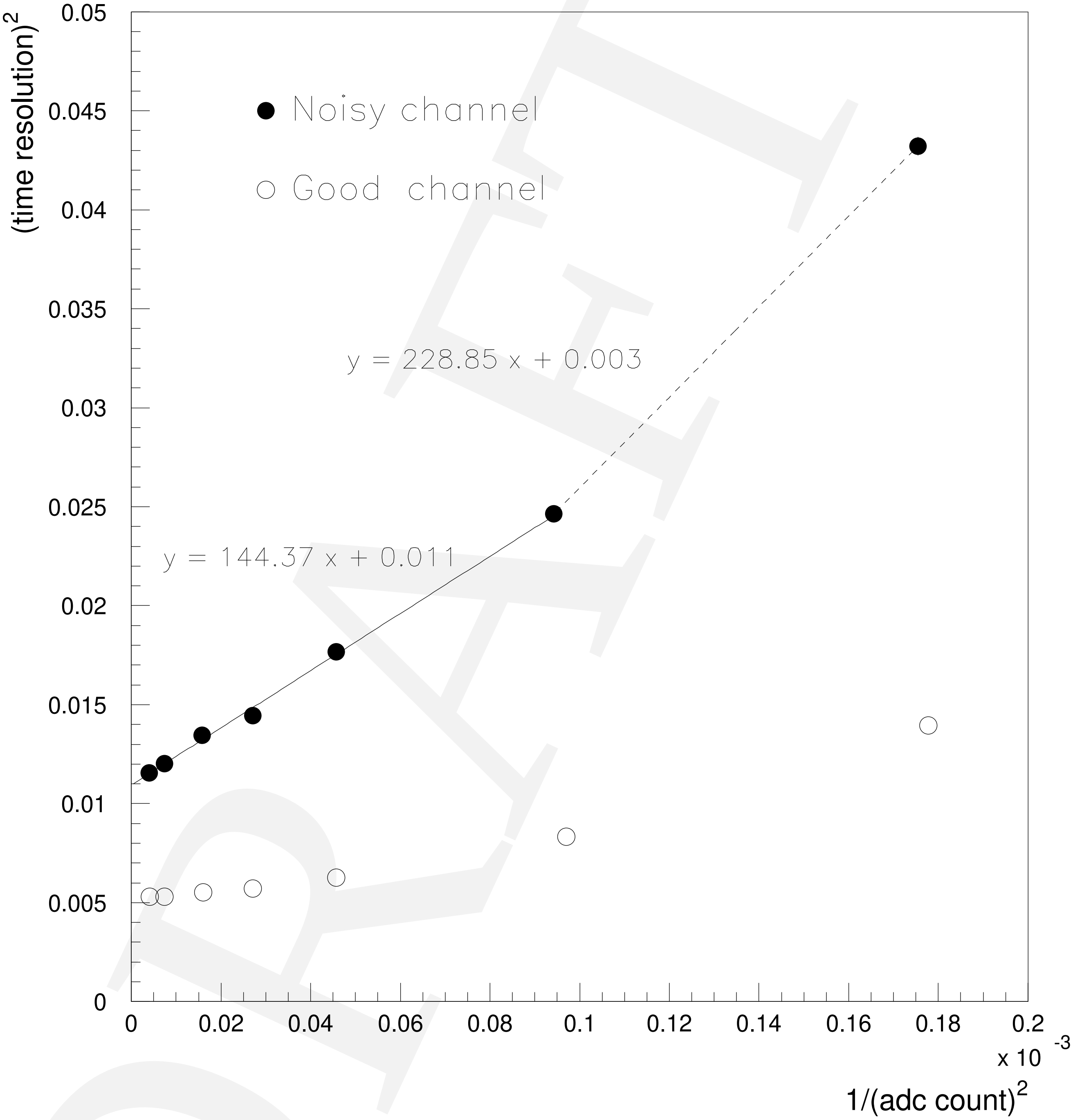

Figure 9: Dependence of time resolution on average charge for good and bad (noisy) amplifiers. All points measured at $B = 0$.

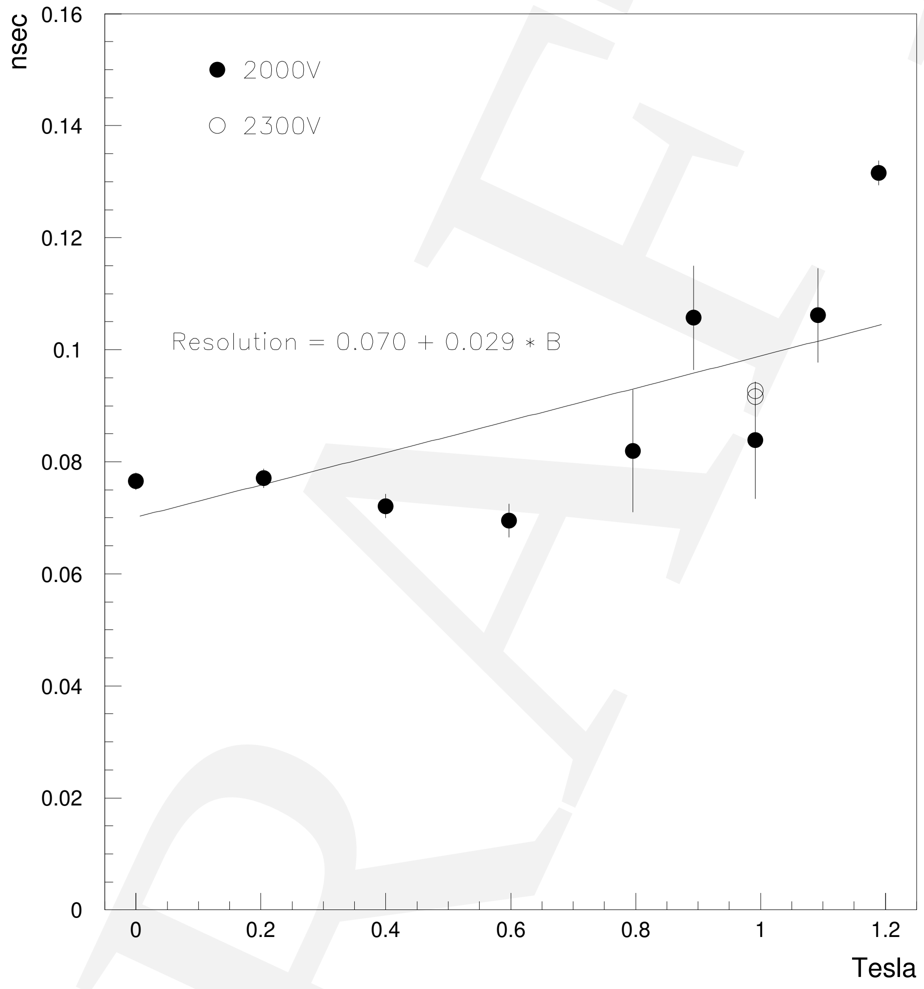

Figure 10: Time resolution vs. magnetic field for the test counter after noise correction.

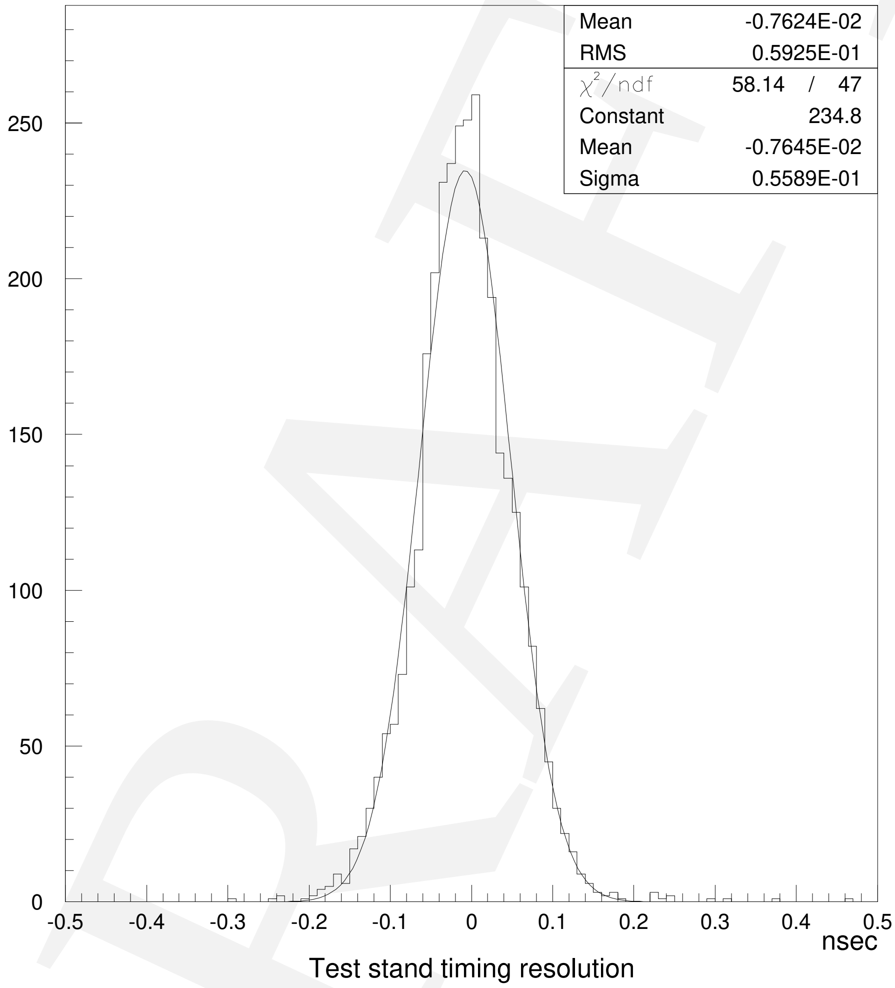

Figure 11: Cosmic ray test stand timing resolution.

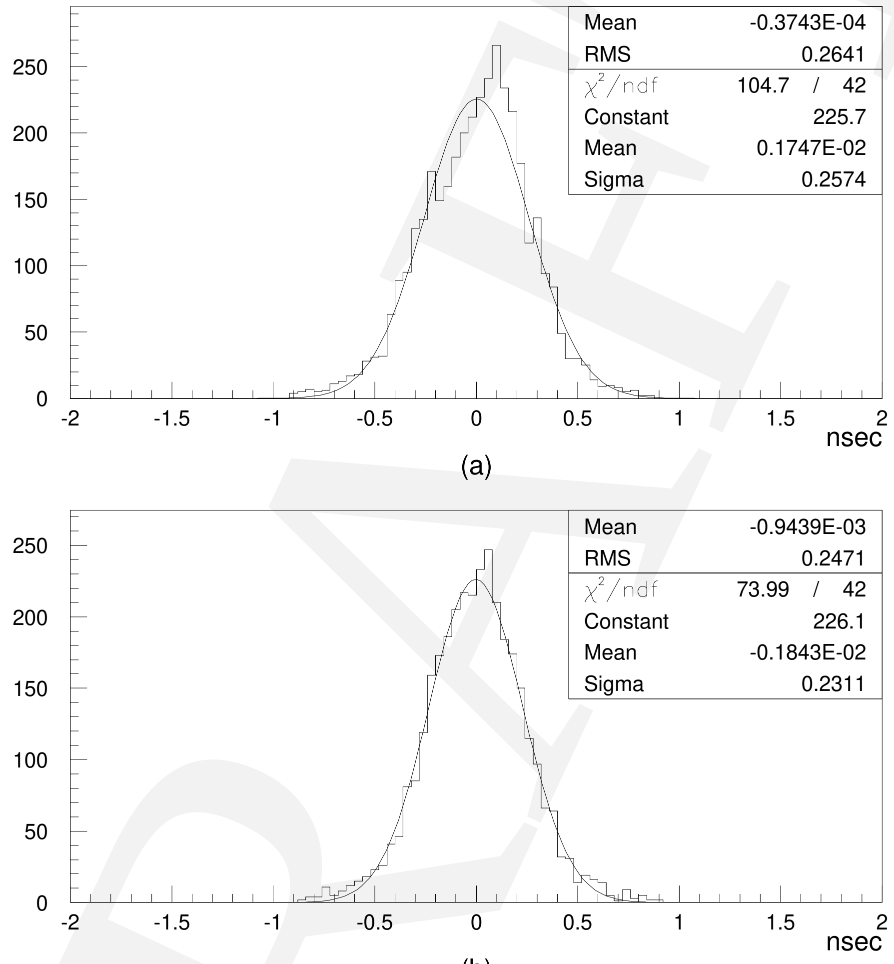

Figure 12: Difference between predicted and measured time for 32 segment prototype counter (a) with reflector and (b) with absorber on the outer scintillator edge.

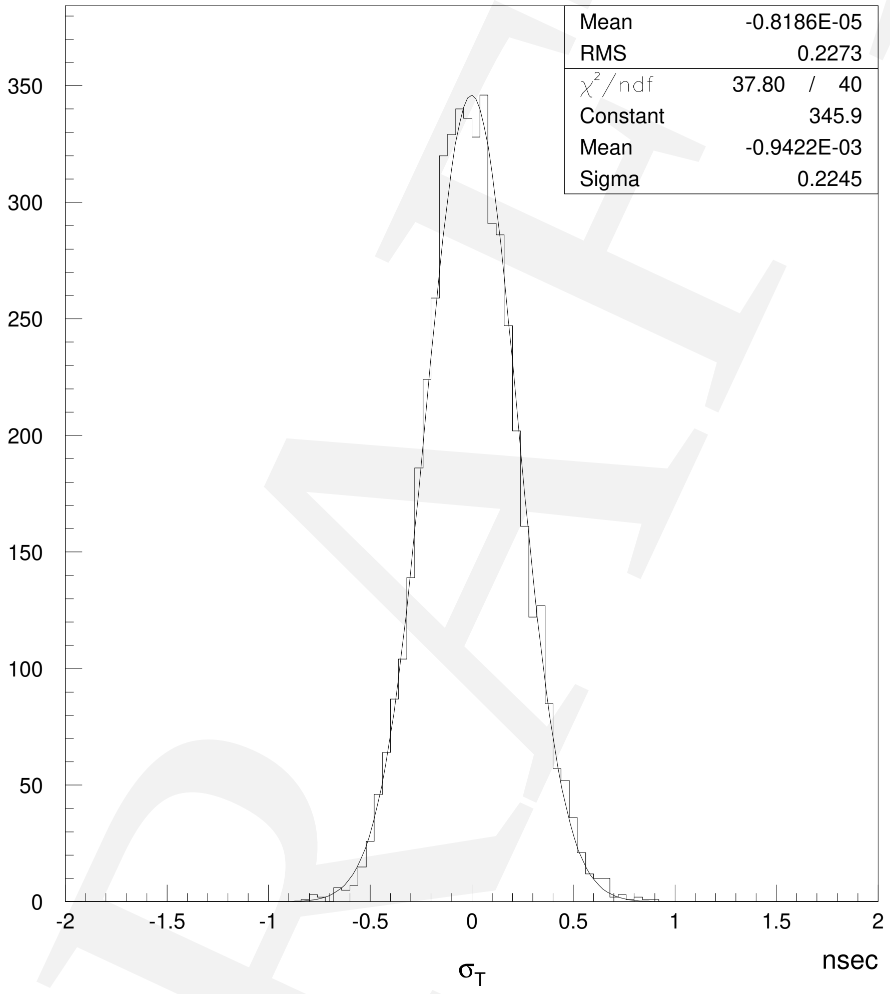

Figure 13: Difference between predicted and measured time for 24 segment prototype counter with absorber on the outer scintillator edge.

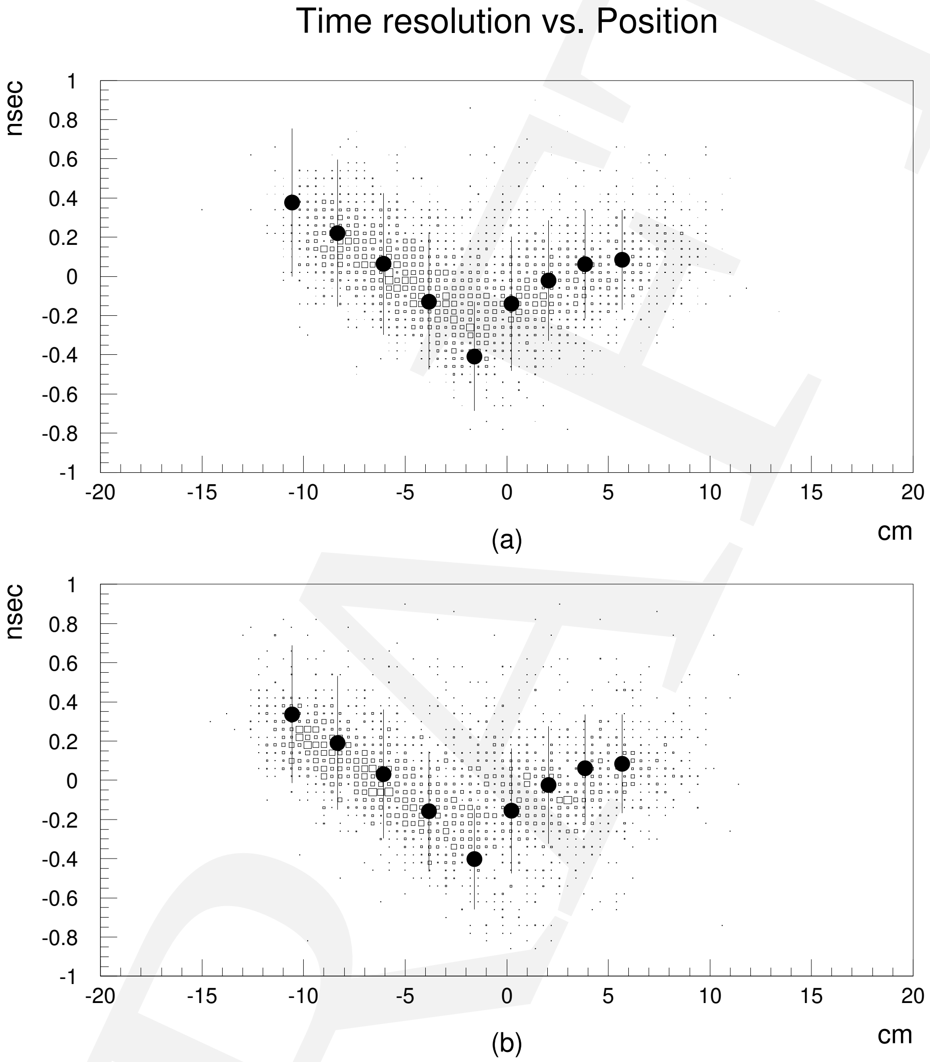

Figure 14: Difference between predicted and measured times vs. charge particle hit position for (a) 24 segment and (b) 32 segment prototype counters with absorber on outer scintillator edge (histogram) overlaid with the predictions of the simulation program (points).

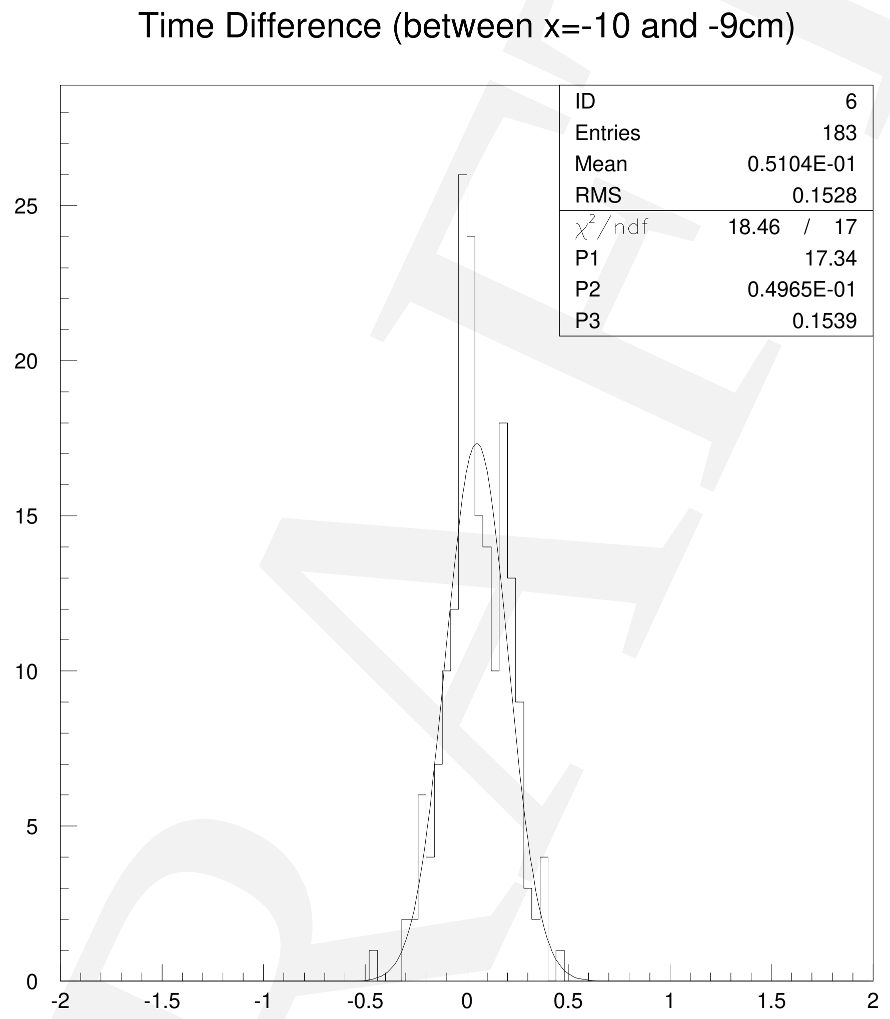

Figure 15: Difference between predicted and measured time for 24 segment prototype counter near the wider end of the scintillator.

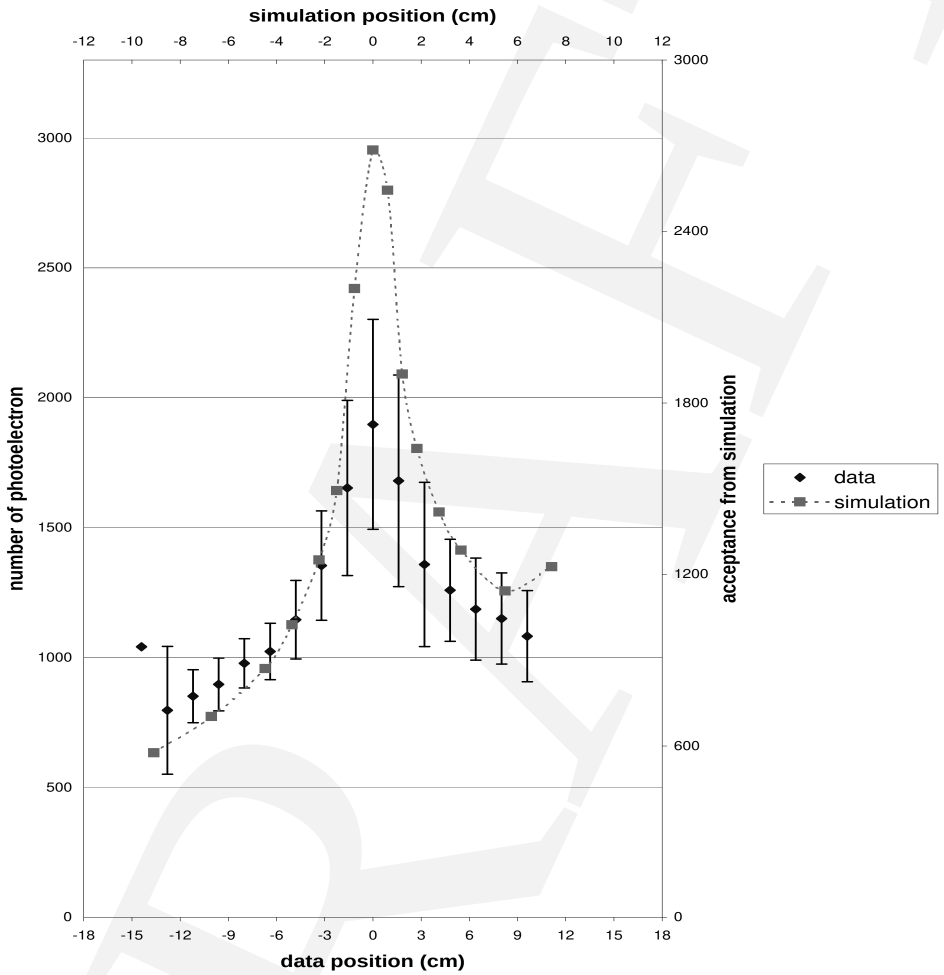

Figure 16: Number of photoelectrons vs. position for 32 segment prototype counter with reflector on the outer scintillator edge.

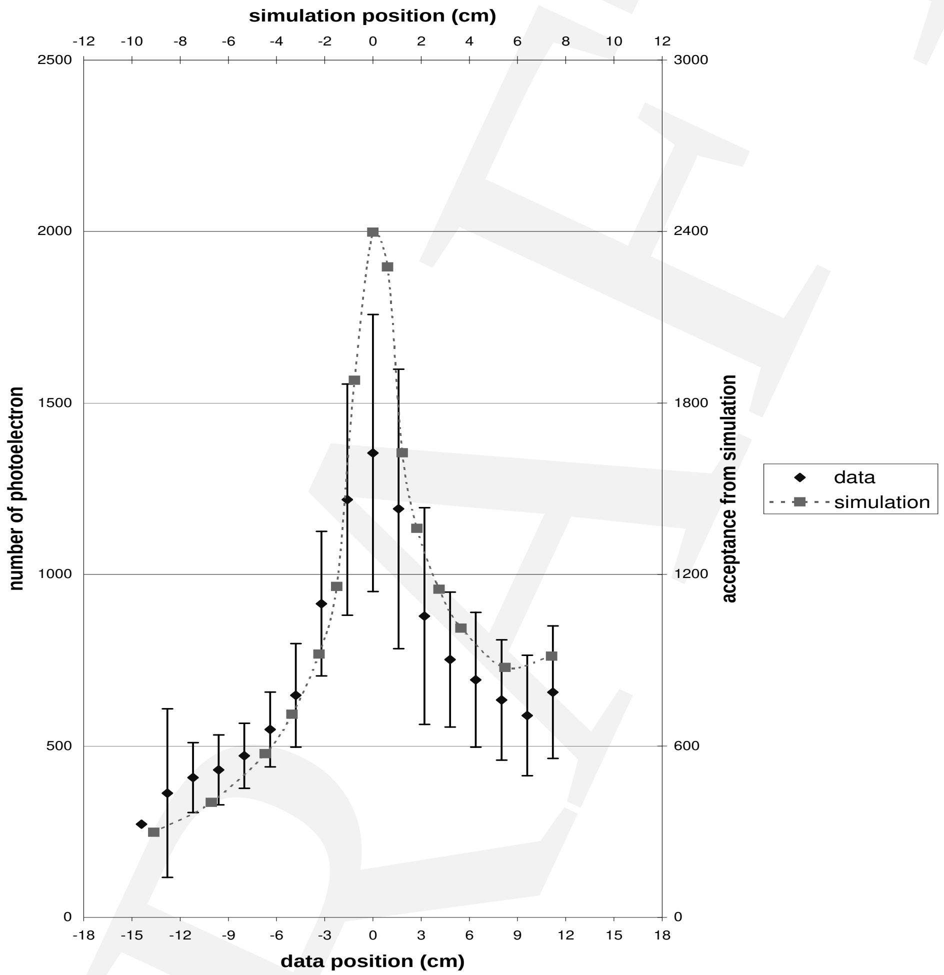

Figure 17: Number of photoelectrons vs. position for 32 segment prototype counter with absorber on the outer scintillator edge.

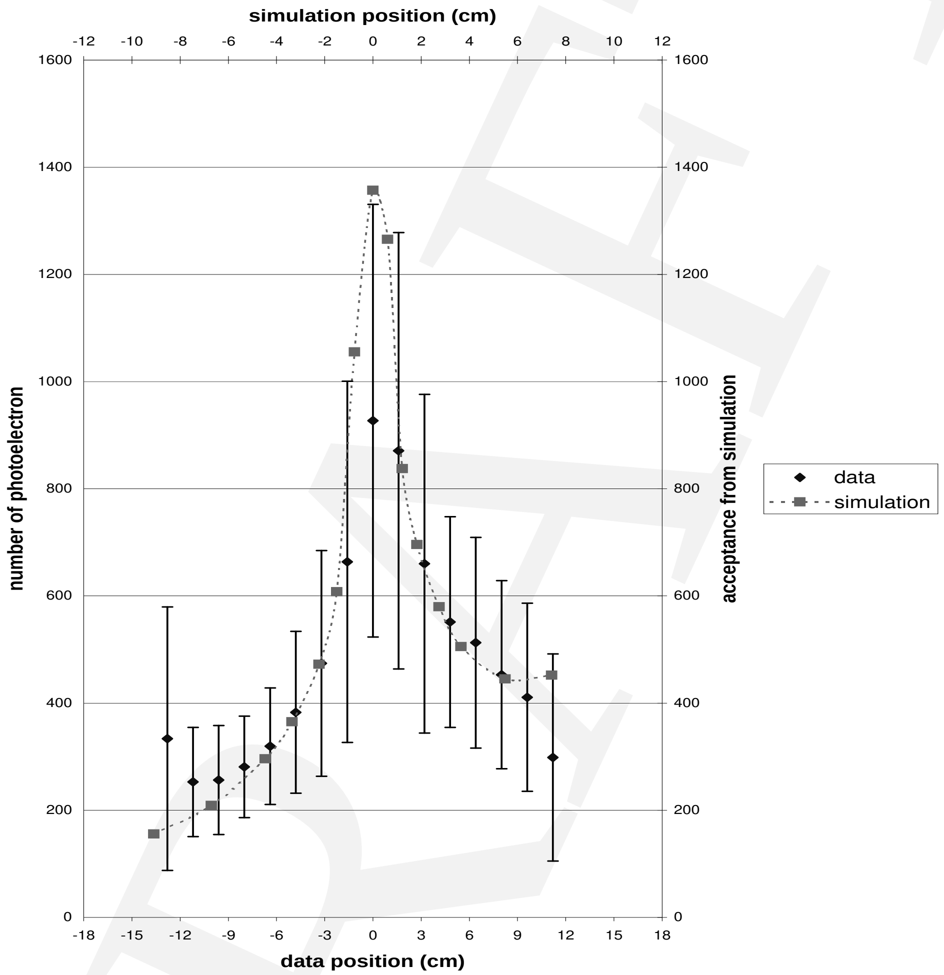

Figure 18: Number of photoelectrons vs. position for 24 segment prototype counter with absober on the outer scintillator edge.